Performance limits due to thermal transport in graphene single-photon bolometers

Caleb Fried, 1,2,3,4,† B. Jordan Russell, 5,† Ethan G. Arnault, Bevin Huang, Gil-Ho Lee, Dirk Englund, Erik A. Henriksen, 5 and Kin Chung Fong, **

 $^{^{7}}$ Department of Physics, Pohang University of Science and Technology, Pohang 790-784, Republic of Korea



(Received 31 October 2023; revised 13 December 2023; accepted 15 December 2023; published 4 January 2024)

In high-sensitivity bolometers and calorimeters, the photon absorption often occurs at a finite distance from the temperature sensor to accommodate antennas or avoid the degradation of superconducting circuitry exposed to radiation. As a result, thermal propagation from the input to the temperature readout can critically affect detector performance. In this paper we model the performance of a graphene bolometer, accounting for electronic thermal diffusion and dissipation via electron-phonon coupling at low temperatures in three regimes: clean, supercollision, and resonant scattering. Our results affirm the feasibility of a superconducting readout without Cooper-pair breaking by mid- and near-infrared photons, and provide a recipe for designing graphene absorbers for calorimetric single-photon detectors. We investigate the trade-off between the input-readout distance and detector efficiency, and predict an intrinsic timing jitter of approximately 2.7 ps. Based on our result, we propose a spatial-mode-resolving photon detector to increase the communication bandwidth.

DOI: 10.1103/PhysRevApplied.21.014006

I. INTRODUCTION

Bolometers are high-sensitivity direct detectors of electromagnetic radiation that sense the temperature rise of a material resulting from photon absorption. Their remarkable sensitivity and broad spectral bandwidth have found numerous applications across various fields, including radio astronomy, spectroscopy, and the observation of rare events like dark matter interactions [1,2]. More recently, bolometers have demonstrated an alternative approach to the traditional heterodyne technique for measuring superconducting qubits [3]. When bolometers achieve single-photon sensitivity and function as calorimeters, they can provide distinct advantages by playing a crucial role in creating entangled quantum states over long distances [4]. The ability to establish entanglement in a broad electromagnetic spectrum using single-photon bolometers can open

up exciting possibilities for advancing quantum communication and information processing technologies over many different hardware platforms.

Graphene is a nearly ideal material for bolometers [5–15] with potential for single-photon sensitivity [16-22] and use in investigating mesoscopic thermodynamics [19,23,24]. The electronic heat capacity of graphene can be exceptionally small due to its minute density of states, which can approach one Boltzmann constant, k_B , at low temperatures [16,18,25] that allow for a substantial temperature rise from absorbing one photon. As a zero-band-gap semimetal, graphene can absorb photons across an extensive range of the electromagnetic spectrum, spanning from ultraviolet to microwave frequencies [26]. Meanwhile, the electron-phonon (e-ph) coupling in graphene is very weak [27-33] due to the requirement of momentum conservation in a small Fermi surface. Finally, the electron-electron (e-e) interaction time is so fast—approaching the Heisenberg uncertainty limit—that heat is rapidly and efficiently diffused among the electrons [34–36]. This characteristic is pivotal for both maintaining

¹Department of Electrical Engineering and Computer Science, Massachusetts Institute of Technology, Cambridge, Massachusetts 02139

²Department of Earth and Planetary Sciences, Harvard University, Cambridge, Massachusetts 02138, USA
³Department of Physics, Harvard University, Cambridge, Massachusetts 02138, USA

⁴Raytheon BBN, Quantum Engineering and Computing Group, Cambridge, Massachusetts 02138, USA
⁵Department of Physics, Washington University in St. Louis, St. Louis, Missouri, USA

⁶Intelligence Community Postdoctoral Research Fellowship Program, Massachusetts Institute of Technology, Cambridge, Massachusetts 02139

^{*}kc.fong@rtx.com

[†]These authors contributed equally to this work.

well-defined localized temperatures within the material and preserving a significant portion of the photon energy in the electrons by mitigating losses to optical phonons during the hot electron cascade [37,38]. Everything considered, we can attribute these desirable bolometric properties to the unique linear band structure of graphene, which distinguishes it from other materials commonly used in bolometers.

Nevertheless, achieving graphene single-photon bolometers remains a substantial challenge [39] because of the short thermal relaxation time of graphene electrons [40] and the lack of fast and direct readout of the electron temperature [7,9,41], Θ_e . Graphenesuperconductor hybrid components have been developed to address these obstacles, including Josephson junctions [19,23,42], superconducting resonators [20,43], and normal-metal-insulator-superconductor tunnel junctions [16]. But their integration to the photon input is not straightforward because the energy carried by infrared (IR) photons exceeds the superconducting gap, leading to the breaking of Cooper pairs that degrades the bolometer performance. One particular crucial design consideration is the distance separating the superconducting readout elements and the location of incoming photon (see Fig. 1). As with transition edge sensors, the thermal properties of the photon absorber can strongly impact the performance of a single-photon bolometer, e.g., jitter, detection speed, dead time, efficiency, and dark count. Previously, the heat diffusion and dissipation in graphene was studied with continuous heating or high optical fluence in the pump-probe experiments at higher temperatures [36,37,44–47]. In contrast, here we report on the electronic thermal transport from the heat of a single photon at low temperatures.

We study the performance of graphene single-photon bolometers resulting from the dissipative thermal diffusion

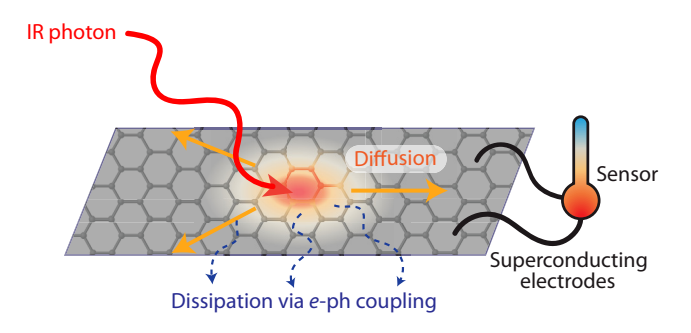


FIG. 1. Schematic of an infrared graphene bolometer. The bolometer comprises a graphene sheet and a thermal sensor readout. When a single infrared photon is absorbed in the graphene, the electron temperature is elevated in a localized hotspot. Heat spreads by thermal diffusion and ultimately dissipates into the lattice via *e*-ph coupling. A superconductor-based sensor can measure the temperature rise, but must be isolated from the photon input to avoid degradation by photon-induced Cooper pair breaking.

towards the superconducting readout. In Sec. II, we introduce the differential equations that govern such processes, the initial and boundary conditions, and the different *e*-ph coupling regimes in graphene. In Sec. III, we solve the one-dimensional (1D) problem using an exact analytical solution for a toy model, before turning to numerical simulations in Sec. IV. Then, we calculate the performance of graphene bolometers (Sec. V) and extend our model to quasi-one-dimension to account for the finite width of a graphene absorber (Sec. VI). We conclude with an outlook envisioning a spatial-mode-resolving detector based on these results.

II. DISSIPATIVE HEAT DIFFUSION OF GRAPHENE ELECTRONS

We begin by considering the dissipative heat diffusion model depicted in Fig. 1, with the absorption of a photon into a graphene sheet with a superconducting readout nearby. We take the incoming light to be focused to a diffraction-limited spot with its size of the order of the photon wavelength, about λ . The absorption efficiency of graphene is only about 2% for light at normal incidence [26], but this can be enhanced with distributed Bragg reflectors [48], evanescent coupling to a proximitized waveguide [49], or a nanophotonic cavity [40]. For longer wavelength photons, $\lambda > 10~\mu\text{m}$, an antenna can guide and impedance match the incident radiation to the graphene [19,50].

Microscopically, the absorption of a photon in graphene is mediated by the interband excitation of a valence-band electron [33] (see Fig. 2). The excited electron produces a localized hotspot via multiple *e-e* scatterings on a fast timescale [35,36,45,51,52], τ_{e-e} , preempting the loss of energy to optical phonons and creating a locally thermalized distribution of charge carriers with a hotspot temperature, Θ_{hot} . This hotspot diffuses out through the length of the graphene by random thermal motion to reach the superconducting sensor. Meanwhile, the heat is also lost to the phonon bath on a timescale $\tau_{e-\text{ph}} \gg \tau_{e-e}$. Our model only considers timescales much longer than τ_{e-e} .

A. Electronic thermal diffusion and dissipation

We establish the differential equation, including diffusion and dissipation to describe the thermal propagation of electrons in graphene. In a small area \mathcal{A} , heat can either diffuse out or dissipate to the lattice via e-ph coupling according to

$$c_e \frac{\partial \Theta_e}{\partial t} = \nabla \cdot (\kappa_e \nabla \Theta_e) - \Sigma (\Theta_e^{\delta} - \Theta_0^{\delta}). \tag{1}$$

The left-hand side of Eq. (1) is the rate of change of the internal energy of the electrons, with c_e and Θ_e the electronic specific heat per unit area and the electronic temperature, respectively. In monolayer graphene, the Fermi

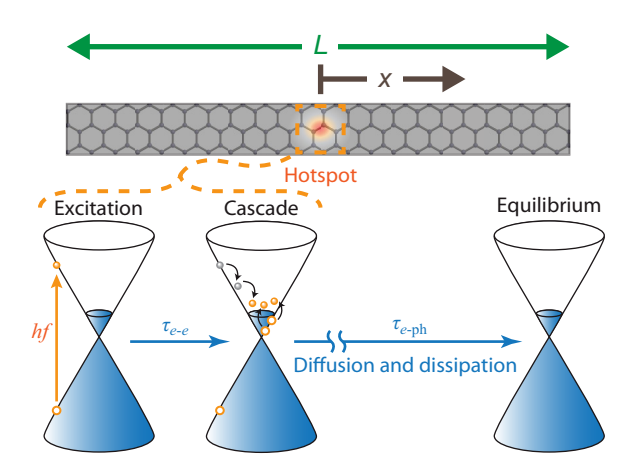


FIG. 2. Photoexcitation cascade and timescales for diffusion and dissipation of electronic heat. The interband excitation from the absorption of an infrared photon with energy hf leads to a cascade of multiple electron-electron scattering events over a time $\tau_{e-e} \sim 100$ fs. This generates a local hotspot of radius ξ , the initial condition in our model. The timescale over which electrons thermalize to the base temperature via e-ph scattering, τ_{e -ph, can be several orders of magnitude longer. During this time, heat spreads through the graphene by electron diffusion and dissipates into the lattice by e-ph coupling. The rise and fall of the electronic temperature at a distance x away from the hotspot can be measured in a graphene sample of length L.

energy $E_F = \hbar v_F k_F$ has a Dirac-like dispersion relation, where $\hbar = h/2\pi$ is the reduced Planck constant, $v_F = 10^6$ m/s is the Fermi velocity, and $k_F = \sqrt{\pi n}$ is the Fermi wave vector with n the charge carrier density. For typical 2D charge carrier densities of 10^{10} – 10^{12} cm⁻², the Fermi temperature, $T_F = E_F/k_B$, ranges from 135 to 1350 K, far higher than typical bolometer operating temperatures of about 1 K. In this degenerate regime the electronic specific heat is a linear function of temperature, $c_e = \gamma \Theta_e$, where $\gamma = 4\pi^{5/2} k_B^2 n^{1/2}/(3hv_F)$ is the Sommerfeld coefficient. The corresponding density of states is $g(E_F) = 2|E_F|A/(\pi \hbar^2 v_F^2)$, growing linearly with E_F measured from the charge neutrality point [26]. This contrasts with the constant density of states in 2D electron gases with parabolic bands, and leads to an extraordinarily small specific heat $c_e \sim 1 k_B/\mu \text{m}^2$ at 20 mK.

The first term on the right-hand side of Eq. (1) is the divergence of the heat flow into or out of \mathcal{A} . By Fourier's law, the heat flow is $-\kappa\nabla\Theta_e$ with κ_e the electronic thermal conductivity. Per the Wiedemann-Franz relation, $\kappa_e = \sigma_e \mathcal{L}_0\Theta_e$, where σ_e is the electrical conductivity and $\mathcal{L}_0 = \pi^2 k_B^2/3e^2$ is the Lorenz number with e the electron charge.

The second term on the right-hand side of Eq. (1) describes the heat transfer per unit area between electrons and the lattice via *e*-ph coupling [30,32,33]. Similar to the Stefan-Boltzmann black-body radiation, it is a high power law in temperature, originating from the integral of bosonic and fermionic occupations and densities of states

in a Fermi golden-rule calculation. Here Σ is the *e*-ph coupling parameter and δ is the constant exponent of a temperature power law that depends on the sample quality.

In Eq. (1), we have omitted the heat flow from the thermoelectric effect [33]. This simplification is justified by the negligible magnitude of the Seebeck coefficient at low temperatures according to the Mott relation [53]. At room temperatures, however, the thermoelectric effect is a sizable effect that can be used as a readout for a bolometer or photodetector [6,13,54].

B. Three regimes of e-ph coupling

A key advantage of graphene is the weak e-ph coupling in Eq. (1), which reduces heat dissipation to maintain a high Θ_e for a long enough time to enable a high signal-to-noise ratio of the Θ_e readout. The strength of the e-ph coupling, i.e., both Σ and δ , can depend on the temperature and cleanliness of the graphene flake. Here, we only consider the e-ph coupling to acoustic phonons because optical phonons in graphene have energies of about 0.2 eV, well above the bolometer operating temperatures [26,37]. For the same reason, we ignore the cooling channel by the surface phonons [33,55,56] as well.

The character of e-ph coupling differs when the electronic temperature is above or below the Bloch-Grüneisen temperature, $\Theta_{BG} = 2\hbar s k_F / k_B$, where s is the sound velocity in graphene [30]. For $T < \Theta_{BG}$, the average phonon momentum is smaller than the size of the Fermi surface, so the accessible momentum space for e-ph scattering is greatly reduced by the need to conserve momentum [30,57,58]. As a result, heat deposited in electronic degrees of freedom can remain trapped for an extended period of time, propagating efficiently across micrometer-scale devices with little loss to the lattice. At the carrier densities $n \sim 10^{12} \, \mathrm{cm}^{-2}$ considered in this work, $\Theta_{\mathrm{BG}} \approx 100 \, \mathrm{K}$. Therefore, we only consider the e-ph coupling below Θ_{BG} , and in three regimes of sample quality: (1) the clean limit, where impurities are scarce and e-ph coupling is weak, (2) the supercollision regime, where disorder enhances e-ph coupling, and (3) resonant scattering, where edge defects enhance e-ph coupling.

The clean limit can be experimentally achieved in pristine, hexagonal-boron-nitride- (h-BN) encapsulated graphene at low temperatures. In these devices the mean free path, $l_{\rm mfp} = \hbar \mu k_F/e$, of charge carriers is longer than the typical inverse phonon momentum. This limit is characterized by a $\delta = 4$ power-law dependence and $\Sigma = \pi^{5/2} k_B^4 D^2 n^{1/2}/(15 \rho_m \hbar^4 v_F^2 s^3)$, with $D \simeq 18$ eV the deformation potential and $\rho_m = 7.4 \times 10^{-19}$ kg μ m⁻² the mass density of graphene. In real devices, this regime is often reported when the perimeter-to-area ratio of the graphene flake is small [18,47,59,60].

Disorder can enhance the *e*-ph coupling by relaxing the constraints on momentum conservation in a process

known as supercollision cooling [31,32]. This regime is characterized by a disorder temperature, $\Theta_{\rm dis}=hs/k_Bl_{\rm mfp}$. When $\Theta_e<\Theta_{\rm dis}$, disorder relaxes the momentum conservation requirement by mediating the scattering process. This enhances the heat transfer between electrons and phonons by a transition to a $\delta=3$ power law and $\Sigma=2\zeta(3)k_B^3D^2n^{1/2}/(\pi^{3/2}\rho_m\hbar^3v_F^2s^2l_{\rm mfp})$, with ζ the Riemann zeta function [32]. In this regime, typically realized in dirty, unencapsulated graphene, hot charge carriers will more rapidly thermalize with the lattice [31,32,61–64].

Scanning temperature probes have revealed a role for a third regime of resonant scattering due to the trapping of hot charge carriers on atomic defects at the edges of the graphene flake [65–67]. The scattering is mostly localized at graphene edges in high-quality encapsulated samples, suggesting that device fabrication may play a role [19,66,68]. Similar to supercollision cooling, the result is an enhancement in e-ph coupling. In this regime, δ is predicted to be either 3 or 5 [67].

For our numerical calculations we employ typical values of numerous graphene material parameters (see Table I) and use experimentally reported values of δ and Σ (see Table II), while noting that more work is needed to confirm the power law and Σ in the resonant-scattering regime for different fabrication methods. In contrast to the clean limit, a power-law scaling of $\delta = 3$ —which may correspond to either the supercollision or the resonant-scattering regime—is typically reported in devices where the graphene is not encapsulated in h-BN or has a large perimeter-to-area ratio [19,52,59,61,63,68,69].

C. Boundary and initial conditions

We use the boundary condition of zero heat flow because the heat diffusion at graphene-superconductor interfaces at temperatures well below the superconducting transition

TABLE I. List of graphene parameters to model single-photon bolometers in this paper. These numerical parameters are taken from various experimental reports [60,63].

Graphene parameters in numerical calculations					
Electron density	n_0	$2.0 \times 10^{12} \text{ cm}^{-2}$			
Electron mobility	μ	$1.0 \times 10^5 \text{ cm}^2 \text{V}^{-1} \text{s}^{-1}$			
Electron mean free path	$l_{ m mfp}$	1.7 μm			
Graphene speed of sound	S	$2.6 \times 10^4 \text{ ms}^{-1}$			
MLG deformation potential	D	$2.9 \times 10^{-18} \text{ J}$			
MLG mass density	$ ho_M$	$7.4 \times 10^{-19} \text{ kg} \mu\text{m}^{-2}$			
Fermi's velocity	v_F	$1.0 \times 10^6 \; \mathrm{ms^{-1}}$			
Electrical conductivity	σ	0.032 S			
Sommerfeld's coefficient	γ	$9.5 \times 10^{-10} \mathrm{Wsm^{-2}K^{-2}}$			
Diffusion constant	\mathcal{D}	$0.82~{\rm m}^2{\rm s}^{-1}$			
Photon frequency	f	193.4 THz			
Photon wavelength	λ	1550 nm			
Base temperature	Θ_0	0.020 K			
Disorder temperature	$\Theta_{ ext{dis}}$	0.73 K			

TABLE II. Different regimes of e-ph coupling in graphene. The $\delta=2$ case, though fictitious, has an analytical solution to Eq. (7) below, making it a useful tool for developing intuition and checking numerical calculations. Numerical parameters for the resonant-scattering regime are estimated from experiments [19,68]. Numerical parameters for the supercollision regime and clean limit are calculated using the parameters in Table I and formulas for Σ in Sec. II B.

Scattering	δ	Σ	$ au_{e ext{-ph}}$	$l_{ m th}$
Fictitious	2			
Resonant [19,68]	3	$1 \text{ Wm}^{-2} \text{K}^{-3}$	16 ns	$114 \mu m$
Supercollision	3	$1.38 \times 10^{-3} \text{ Wm}^{-2} \text{K}^{-3}$	$11 \mu s$	3.1 mm
Clean limit	4	$3.10 \times 10^{-2} \text{ Wm}^{-2} \text{K}^{-4}$	$19 \mu s$	4 mm

temperature can be substantially suppressed, as Cooper pairs carry no thermodynamic entropy and cannot conduct heat [63,70]. Thanks to both theoretical [71] and experimental [35,36,44,45,51,72] efforts, the initial temperature profile of the hotspot after the photon absorption is reasonably understood and will be modeled as a Gaussian distribution with a half width half maximum ξ :

$$\Theta_e(t=0) = \Theta_{\text{hot}}e^{-(x-x_0)^2/2\xi^2} + \Theta_0.$$
 (2)

Here x_0 is the location of the photon absorption, and Θ_{hot} and Θ_0 are the peak hotspot and base temperature, respectively. It will be useful for our analysis to have an initial condition that is Gaussian distributed in Θ_e^2 instead of Θ_e :

$$\Theta_e^2(t=0) = \Theta_{\text{hot}}^2 e^{-(x-x_0)^2/\xi^2} + \Theta_0^2.$$
 (3)

For $\Theta_{hot} \gg \Theta_0$, Eqs. (2) and (3) are approximately equivalent. The average energy of electrons in the hotspot after the initial photoexcitation cascade [37,38] will determine Θ_{hot} . For near-IR photons, this temperature is typically on the scale of hundreds to thousands of kelvins, which is $\gg \Theta_0$, justifying Eq. (3). To estimate Θ_{hot} , we equate the photon energy with the integrated heat capacity with respect to temperature, yielding [23]

$$hf = \int_{\Theta_e}^{\Theta_{\text{hot}}} \pi \xi^2 \gamma \,\Theta_e \, d\Theta_e, \tag{4}$$

$$\Theta_{\text{hot}}^2 = \frac{2hf}{\pi \xi^2 \gamma} + \Theta_0^2. \tag{5}$$

Here $\Theta_{\text{hot}} = 100 \text{ K}$ corresponds to $\xi = 94 \text{ nm}$, which is consistent with values previously reported in the literature [36,73]. Since ξ is much smaller than the size of the graphene flake, the initial heating profile is effectively a point source in our model.

D. Simplifying to one dimension

As we are interested in how to keep the photon input far enough from the superconducting electrodes of the readout circuit to avoid Cooper pair breaking, the optimal aspect ratio of our graphene bolometer would be a long strip, as depicted in Fig. 2, to minimize the total heat capacity. Therefore, we simplify our dissipative heat diffusion differential equation, Eq. (1), to one dimension, i.e.,

$$\gamma \Theta_e \frac{\partial \Theta_e}{\partial t} = \frac{\partial}{\partial x} \left(\sigma \mathcal{L}_0 \Theta_e \frac{\partial}{\partial x} \Theta_e \right) - \Sigma (\Theta_e^{\delta} - \Theta_0^{\delta}), \quad (6)$$

using $c_e = \gamma \Theta_e$ and the Wiedemann-Franz law. Furthermore, we can rewrite the equation in terms of Θ_e^2 to obtain

$$\frac{\partial}{\partial t}\Theta_e^2 = \mathcal{D}\frac{\partial^2}{\partial x^2}\Theta_e^2 - \frac{2\Sigma}{\nu}(\Theta_e^\delta - \Theta_0^\delta),\tag{7}$$

in which we define a diffusion constant $\mathcal D$ such that

$$\mathcal{D} = \frac{\sigma \mathcal{L}_0}{\gamma} = \frac{E_F \mu_e}{2e},\tag{8}$$

where μ_e is the electron mobility, $\mu_e = \sigma/ne$, and Eq. (8) is the Einstein relation [36,74]. For $\mu_e \simeq 10^5$ cm²V⁻¹s⁻¹ and density 2.0×10^{12} cm⁻², the typical σ value is 0.032 S, giving a numerical value for \mathcal{D} of 0.82 m²s⁻¹, which is consistent with measured values [36,44]. In general, this nonlinear diffusion equation has no analytical solution for arbitrary values of δ , with the exception of some special cases.

III. ANALYTIC DESCRIPTION OF THE $\delta=2$ CASE

We can analytically solve Eq. (7) when $\delta = 2$ and the graphene sample is infinitely long. Using the initial condition, Eq. (4), with $x_0 = 0$, the solution is

$$\Theta_{e}(x,t) = \left[\Theta_{0}^{2} + e^{-t/\tau_{e-ph}} e^{-(x-x_{0})^{2}/(\xi^{2} + 4\mathcal{D}t)} \times \frac{\Theta_{\text{hot}}^{2}}{\sqrt{1 + 4\mathcal{D}t/\xi^{2}}}\right]^{1/2},$$
(9)

where $\tau_{e\text{-ph}}^{(\delta=2)} = \gamma/2\Sigma$ is the thermal time constant bottle-necked by e-ph coupling when $\delta=2$. While the first term, Θ_0^2 , comes from the base temperature, the second term describes the rise and fall of Θ_e , within which the first exponential-decay factor is due to the e-ph coupling with time constant $\tau_{e\text{-ph}}$. When there are additional channels of heat dissipation, such as radiative coupling or contact to normal-metal electrodes, we can replace $\tau_{e\text{-ph}}$ with a more general thermal time constant, τ_{th} . We have $\tau_{th} \leq \tau_{e\text{-ph}}$ because additional conductance channels will speed up the thermal dissipation. In the linear response regime, τ_{th} is given by the ratio of specific heat to the total thermal conductivity [23]. The second factor provides the initial

rise of temperature at position x from the source at x_0 due to diffusion of heat, while the third factor describes the fall of Θ_e as heat diffuses further away.

Figure 3 plots Eq. (9) with increasing Σ from Figs. 3(a) to 3(c). When diffusion dominates [Fig. 3(a)], the heat can diffuse throughout the sample. At a position x, the temperature will rise at $t \simeq (x-x_0)^2/\mathcal{D}$, and subsequently fall with a power law of $t^{-1/4}$. The latter is the expected diffusive behavior, i.e., $\Theta_e^2 \propto 1/\sqrt{t}$, in contrast to $\Theta_e \propto 1/\sqrt{t}$ if both c_e and κ_e do not depend on Θ_e . As dissipation rises, we can still observe diffusive behavior when $t < \tau_{e\text{-ph}}$, but Θ_e falls at a faster rate than $t^{-1/4}$ [Fig. 3(b)] because of the high-temperature power law of δ . The electron temperature Θ_e decays at $\simeq \tau_{e\text{-ph}}^{(\delta=2)}$, independent of the position x. Deeper in the e-ph dominated regime, the decay timescale is fast enough to compete with the initial temperature rise from thermal diffusion [Fig. 3(c)]. In this limit, the heat from the photon may not reach the sensing element of the detector before it is lost to the lattice.

To investigate the thermal behavior of the system at finite size, we solve Eq. (1) numerically for a graphene sheet of length L with a hotspot in its middle. The second column of Fig. 3 plots these numeric solutions alongside the analytic solutions from the first column. Initially, all of these finite-system solutions follow the same initial rise and fall of Θ_e observed in the infinite-system analytic solutions. In the diffusive limit [Fig. 3(d)], the finite-size solutions reach a plateau in temperature after a certain time, with shorter samples settling at a higher temperature than longer samples. From Θ_e at different positions along a 20- μ m sheet plotted in Fig. 3(g), we confirm that Θ_e plateaus when the entire length of the graphene thermalizes to a uniform temperature, $\Theta_{uniform}$. Once the electron temperature is uniform, diffusion is complete and only dissipation can further lower the temperature. We can understand this behavior better by plotting the results in Fig. 4 with the circles in the panel marking the time, $\tau_{uniform}$, at which graphene sheets of different lengths reach the plateau. Figure 4(b) plots τ_{uniform} versus L. Clearly, τ_{uniform} follows the expected behavior for diffusion, $\tau_{\text{uniform}} = (L/2)^2/2\mathcal{D}$ (solid line), where L/2 is the distance from the hotspot to either end of the graphene flake. Evaluating Eq. (9) at $t = L^2/8D$, Fig. 4(c) shows Θ_{uniform} for different L. We can estimate $\Theta_{uniform}$ by considering our analytic solution in the diffusive limit. When $\xi^2/\mathcal{D} \ll t \ll \tau_{e\text{-ph}}$ and $\Theta_{\text{hot}} \gg \Theta_0$, Eq. (9) simplifies to

$$\Theta_e \simeq \frac{\Theta_{\text{hot}}}{(1 + 4\mathcal{D}t/\xi^2)^{1/4}}.$$
 (10)

Substituting τ_{uniform} for t, and the estimation of Θ_{hot} from Eq. (5), we have

$$\Theta_{\text{uniform}} \simeq 2^{3/4} \sqrt{\frac{hf}{\pi \xi L \gamma}}.$$
(11)

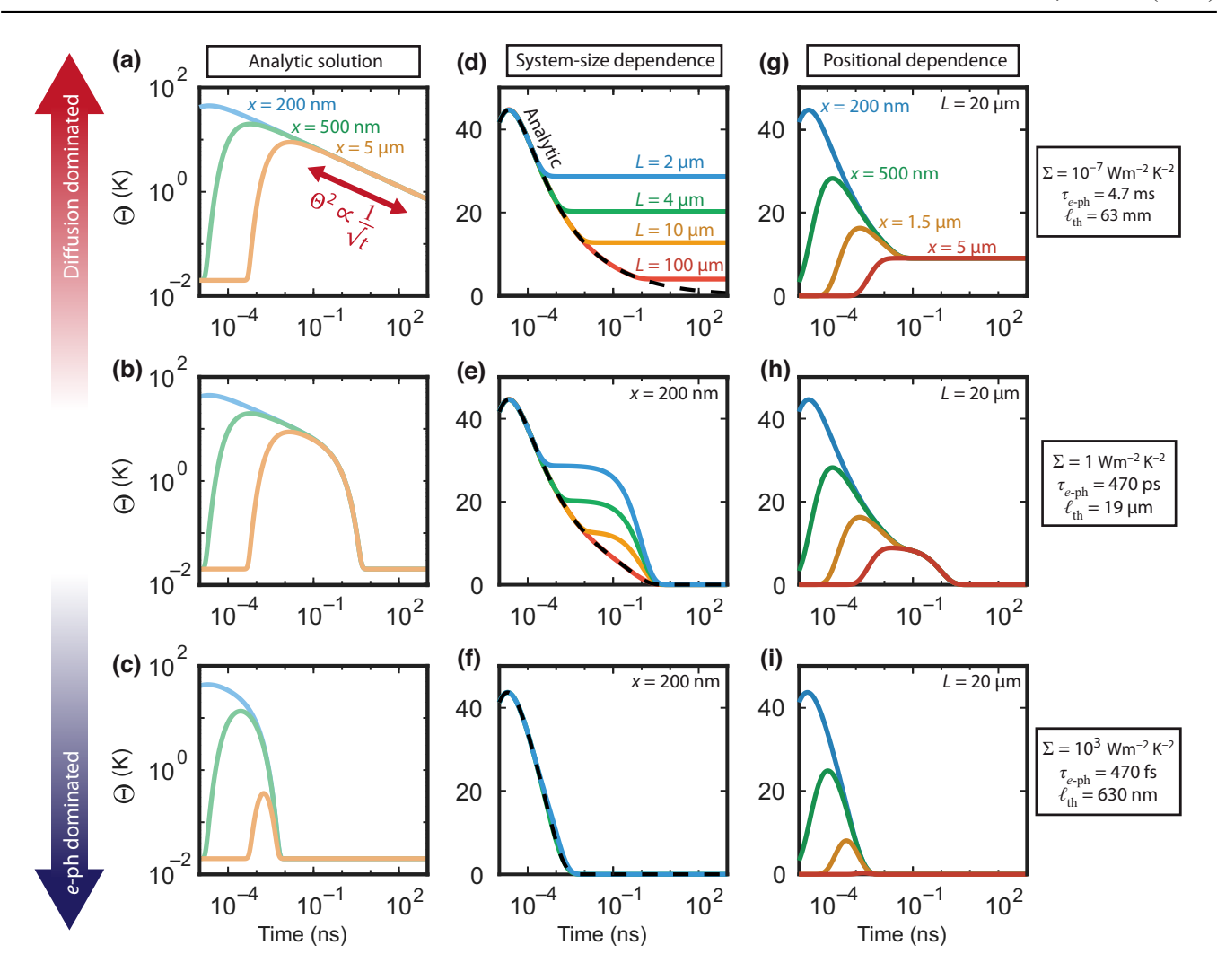


FIG. 3. (a)–(c) Analytic solution for $\delta=2$ in an infinitely long sample—results of numerical calculations of our analytic solution of the one-dimensional heat equation with an e-ph diffusion term. By adjusting the strength of the e-p coupling constant Σ , we can observe three regimes of heat diffusion in graphene. In (a), when the e-ph coupling is weak, the system is dominated by diffusion, characterized by the persistent $1/\sqrt{t}$ power law in Θ^2 . In (c), when the coupling is strong, the thermal propagation is dominated by dissipative e-ph effects. When the two effects are more closely balanced, like in (b), we can see a mix of diffusive and dissipative effects playing out on different timescales. (d)–(f) System size dependence for $\delta=2$: analytic versus numerical solution. Moving from infinitely long samples to graphene of finite length necessitates solving the heat equation numerically. Panels (d)–(f) compare the analytic solution (black dotted line) to the numerical results for various lengths of graphene. The numerical results line up well with the analytic solution for long samples. The plateau in the temperature is explained by the entire sheet of graphene reaching a uniform temperature, which persists for a timescale determined by the e-ph coupling. (g)–(i) Positional dependence in numerical solutions for $\delta=2$. Panels (g)–(i) show the simulated temperature response measured at various lengths away from the hotspot for a photon absorbed in the center of a 20- μ m piece of graphene. Predictably, the heat from the incoming photon takes longer to propagate to spots further away on the graphene. After approximately 100 ps, all locations on the graphene reach a uniform temperature.

Comparison with Eq. (5), Eq. (11) suggests that the factor $\pi \xi L$ is the effective area of the 1D graphene flake, with Θ_{uniform} playing the role of hot-carrier temperature when the photon energy is distributed evenly across the entire graphene. Equation (11) [solid line in Fig. 4(c)] well approximates Θ_{uniform} from our numerical calculation.

In Fig. 3(e), we move beyond the diffusive limit. Here we can still see the plateau behavior, but, similar to Fig. 3(b), the temperature subsides quickly after the

timescale $\tau_{e\text{-ph}}^{(\delta=2)}$. Beyond a certain sample length, however, the timescale of e-ph coupling is faster than the time at which a uniform temperature is reached, so the plateau does not appear. The relevant length scale for this behavior is the thermal-diffusion length $l_{\text{th}} = \sqrt{D\tau_{e\text{-ph}}}$ [37]. In Fig. 3(e), the 100- μ m sample exceeds the l_{th} value of 19 μ m, and so exhibits no plateau behavior. In the e-ph-dominated regime [Fig. 3(f)], the timescale of thermal dissipation is so short that the plateau behavior is never

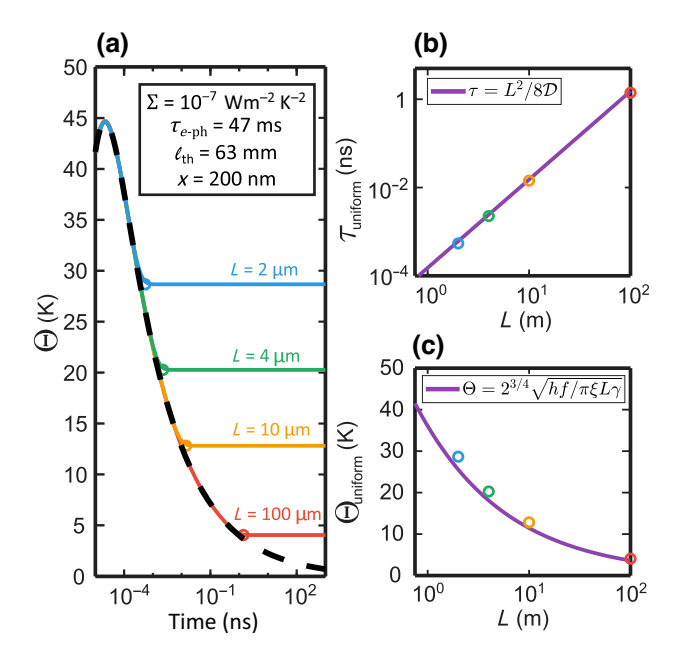


FIG. 4. Diffusive behavior for $\delta=2$ —numerical calculations showing the details of the temperature plateau seen in the diffusive limit. (a) Equivalent to Fig. 3(d), the behavior of different lengths of graphene in different colors (with the analytic solution for a sample of infinite length plotted as a dashed black line). (b) The timing of the plateau behavior τ_{uniform} plotted against the sample length L, which follows $L^2/8\mathcal{D}$, characteristic of diffusion. (c) The temperature of the plateau Θ_{uniform} against the system length, which is predicted by Eq. (10).

observed for the sizes of the graphene that we consider in this paper.

Lastly, Figs. 3(g)–3(i) plot Θ_e at different positions for $L=20~\mu m$. In the intermediate regime, Θ_e reaches $\Theta_{uniform}$ before relaxing back to Θ_0 , following the same curve governed by e-ph coupling regardless of the position. In the dissipative regime [Fig. 3(i)], a uniform elevated temperature is never reached, since the timescale of e-ph coupling, τ_{e -ph, is faster than the time $L^2/4\mathcal{D}$ required for diffusion to bring the graphene to a uniform temperature.

IV. SOLUTION FOR $\delta = 3$ AND $\delta = 4$

A. Linearized differential equation

Although there is no exact solution to the dissipative heat diffusion differential equation [Eq. (7)] for $\delta = 3$ or 4, we can gain more insight by linearization. Using the substitution of $u = \Theta^2$ to Taylor expand Eq. (7), we find that

$$\frac{\partial u}{\partial t} = \mathcal{D}\frac{\partial^2 u}{\partial x^2} - \frac{2\Sigma}{\gamma}(u^{\delta/2} - u_0^{\delta/2}) \tag{12}$$

$$\simeq \mathcal{D}\frac{\partial^2 u}{\partial x^2} - \frac{\delta \Sigma u_0^{\delta/2-1}}{\gamma} (\Delta u + \cdots), \qquad (13)$$

where $\Delta u = u - u_0$. While Eq. (12) is still exact, the linearization [Eq. (13)] contains an approximation for the dissipative term. Taking only the first term of the Taylor expansion, Eq. (13) becomes linear in u. As a result, the solution takes the exact same form as Eq. (9), but with a more general form for $\tau_{e\text{-}ph}$:

$$\tau_{e\text{-ph}} = \frac{\gamma}{\delta \Sigma \Theta^{\delta - 2}}.$$
 (14)

As a result, most of the intuition built up in Sec. III is applicable to the more realistic $\delta = 3$ and 4 cases, especially in the diffusion-dominated regime.

We plot the linearized analytic solutions for each regime in Fig. 5. The timing and magnitude of the initial peak in temperature track closely, i.e., $t \ll \tau_{e\text{-ph}}$, across all e-ph regimes because the diffusion term in Eq. (13) is independent of δ and Σ . On the other hand, Θ_e drops differently depending on e-ph regimes with the time constant given by Eq. (14). The linearized analytic solutions are ordered from fastest to slowest e-ph dissipation time according to their power law, with $\delta=2$ the most dissipative and $\delta=4$ the least dissipative. However, the magnitude of Σ also plays a considerable role in determining the behavior of each regime: for instance, there is a greater difference between the two $\delta=3$ regimes than between $\delta=3$ and $\delta=4$.

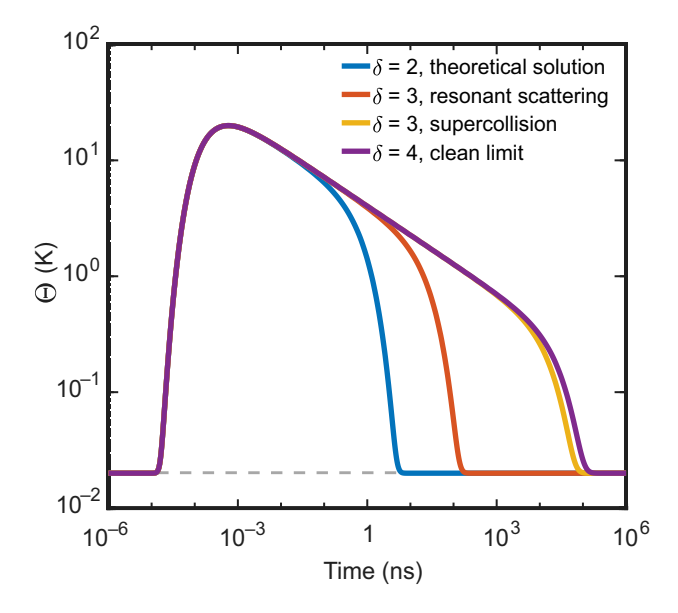


FIG. 5. Analytic solution of the linearized differential equation for $\delta=3$ and 4 for an infinitely long sample. We plot analytical calculations showing the different thermal responses of graphene following $\delta=4$ versus $\delta=3$ power laws, alongside a purely theoretical $\delta=2$ solution. For these calculations, we set $\Sigma=1$ for the $\delta=2$ case, representing the regime in between diffusive and dissipative. The values of Σ for the $\delta=3$ and $\delta=4$ cases are shown in Table II. Temperatures are measured at a distance of x=1 μm away from the hotspot.

Specifically, we have used a relatively clean graphene, with an electron mobility of 10^5 cm²/Vs and an $l_{\rm mfp}$ of $1.7 \,\mu \text{m}$, even in the supercollision regime.

B. Numerical solutions

Similar to Figs. 3(d)–3(i), Fig. 6 shows the numerical solutions to Eq. (7) for a finite-sized graphene. In the supercollision regime [Fig. 6(a)], Θ_e behaves similarly to the diffusive limit of $\delta=2$, where Θ_e plateaus as the entire graphene reaches a uniform temperature, and Θ_{uniform} and τ_{uniform} depend on the system size in the same manner as shown in Fig. 4. In contrast, the shorter or vanishing plateaus of the clean and resonant-scattering regimes imply a weaker diffusive behavior [Figs. 6(b) and 6(c)], leading to a drop to the baseline temperature faster than the linearized analytic solution. We emphasize that the qualitative behavior of Θ_e depends on both the numerical values of Σ and δ , rather than just the assignment of an e-ph scattering regime, as elaborated below.

Contrary to the behavior of the linearized analytic solution plotted in Fig. 5, the $\delta = 3$ supercollision scattering mechanism exhibits much more diffusive behavior than the $\delta = 4$ clean limit when using the same numerical parameters. This is because $\Theta_e \gg \Theta_0$ in these calculations, well outside the linear response. The higher power-law dissipation can relax Θ_e with a timescale, $\tau_{\rm relax}$, that depends on both δ and Σ . We expect $\tau_{\text{relax}} < \tau_{\text{th}} \le \tau_{e\text{-ph}}$. As illustrated in Fig. 5, the value of τ_{e-ph} for the supercollision regime is slightly shorter than for the clean regime given the experimental conditions and parameters in Table I. But the lower power law means that τ_{relax} for the $\delta = 3$ supercollision regime is longer than the $\delta = 4$ clean regime when $\Theta_e \gg$ Θ_0 . This is the reason for the stronger diffusive behavior observed in the supercollision regime [Figs. 6(a) and 6(d)] compared to the clean regime [Figs. 6(b) and 6(e)]. On the other hand, the numerical value of Σ is several orders of magnitude larger for the resonant-scattering regime (see Table II), so that it exhibits the least diffusive behavior of the three regimes, despite having both a lower power law than the clean regime and a shorter $\tau_{\rm relax}$. This result demonstrates the need to numerically solve the dissipative heat diffusion differential equation because qualitative details can depend on the experimental values of both Σ and δ . The same intuition for the faster-than-exponential dissipation for high power laws in the e-ph coupling can also explain why the numerical solutions drop below the analytic solution in linear response (black dotted line in Fig. 6).

The position dependence of Θ_e for $\delta=3$ and 4 [Figs. 6(d)–6(f)] behaves similarly to the $\delta=2$ solutions. For the supercollision regime, in Fig. 6(d) we plot the different locations on a graphene flake reaching Θ_{uniform} , maintaining it for a time, and eventually subsiding to Θ_0 . The electron temperature Θ_e in

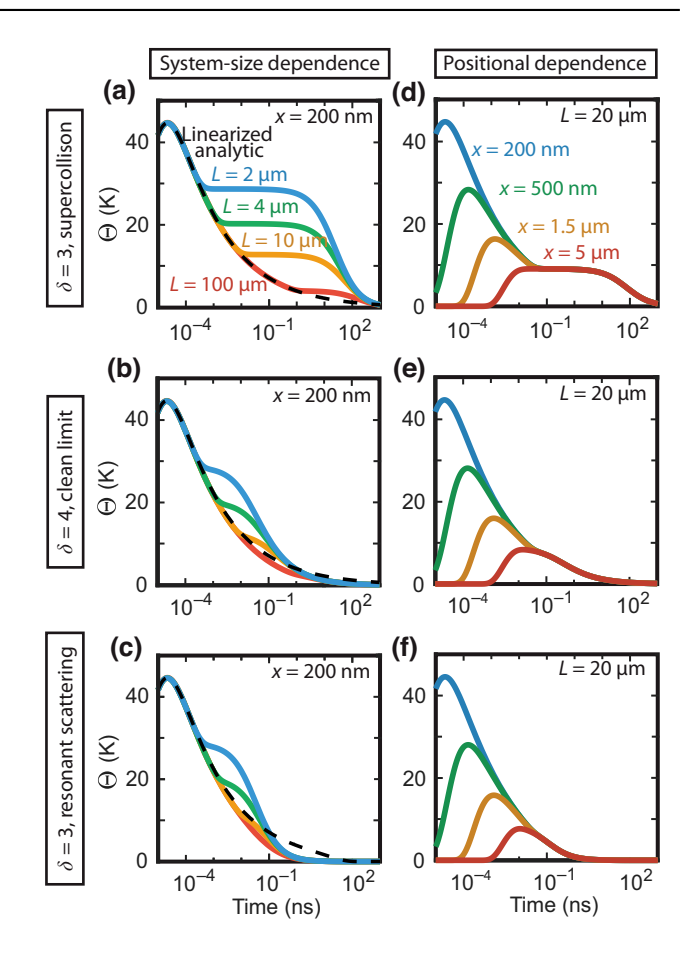


FIG. 6. The size dependence of the numerical solution for $\delta=3$ and 4 for a finite-sized sample. (a)–(c) The numerical simulation results for graphene samples of a variety of different finite sizes for each of the higher power-law *e*-ph coupling regimes, in order from most (panel (a)) to least (panel (c)) diffusive. The temperature response is measured 200 nm away from the hotspot. The linearized analytic solution [Eq. (9) with τ_{e^-ph} given by Eq. (14)] is plotted as a black dashed line. Notably, the more diffusive the system, the better the linearized approximation performs. (d)–(f) The positional dependence of the same three regimes for a 20-μm-long flake of graphene. The resonant-scattering regime exhibits the fastest temperature decay, while the supercollision regime exhibits the slowest.

the clean and resonant-scattering regimes [Figs. 6(e) and 6(f)] can also reach the same Θ_{uniform} as in Fig. 6(d), although the dissipation has already kicked in by the time Θ_e reaches Θ_{uniform} . A subtle but important difference between Figs. 6(e) and 6(f) is the speed at which the sample thermalizes to Θ_0 after $t \simeq \tau_{\text{uniform}}$. The tail of the temperature curve decays with a considerably gentler slope in Fig. 6(e) than in Fig. 6(f), corresponding to several additional nanoseconds at an elevated temperature for a device in the clean regime than for a device in the resonant-scattering regime. This difference will prove to be important to the detector efficiency.

V. BOLOMETER PERFORMANCE LIMITED BY DISSIPATIVE HEAT DIFFUSION

A. Detector efficiency in the mid- and near-infrared regimes

We can now use the calculated $\Theta_e(t)$ at the sensor position, of distance d, from the photon input to study the performance of the graphene bolometer. To begin, we need to choose the heat sensor that will be used because its operation mechanism can determine the overall sensitivity, efficiency, readout bandwidth, dark count, and timing jitter. For example, when applying resonator techniques to directly measure Θ_e in a normalmetal-insulator-superconductor [75] or Josephson junction [76], we expect the bolometer sensitivity to depend on the noise temperature of the amplifier chain of the entire measurement system. On the other hand, when using a Josephson junction to indirectly detect the rise of Θ_e from the switching rate [23,42], one may evade the amplifier noise when the Josephson junction switches discontinuously from the superconducting to resistive state in response to the arrival of a photon. Such a dc measurement is straightforward to implement and we use it to analyze the performance of a single-photon bolometer in this paper. In comparison, the kinetic inductance measurement [77] with a resonator is a faster and probably higher-sensitivity readout to register the fleeting rise and fall of $\Theta_e(d,t)$ due to absorbing a single photon. We defer analysis of the resonator readout to a future work due to additional complexity arising from a τ_{th} that is shorter than the response time of the readout resonator.

Let us now consider the bolometer design. The first criteria is to keep the superconducting readout circuitry and the location of the photon input separated by a distance shorter than the thermal diffusion length, $l_{\rm th}$. This requirement can easily be satisfied because l_{th} is of the order of tens of micrometers, much longer than the photon wavelength. Since the temperature rise from photons scales inversely to the heat capacity, the graphene bolometer must be short in the transverse direction to minimize the total area, while remaining long enough in the longitudinal direction to maintain the separation between the photon input and superconducting readout. Figure 7(a) illustrates the graphene bolometer that we have modeled to assess its detection efficiency in the near- and mid-IR regimes. The photon input, a focused, diffraction-limited light spot with a beam waist of about λ , is located in the middle of the flake while the sensor, a Josephson junction with a graphene weak link, is attached to the end of the flake. We set the length of the graphene absorber to be 2λ to allow for the efficient coupling of photons [40,78]. As the photon wavelength increases from the near-IR to the mid-IR regime, we expect the detector efficiency to decrease. This is because the size of a diffraction-limited beam spot grows with increasing wavelength, requiring a larger graphene

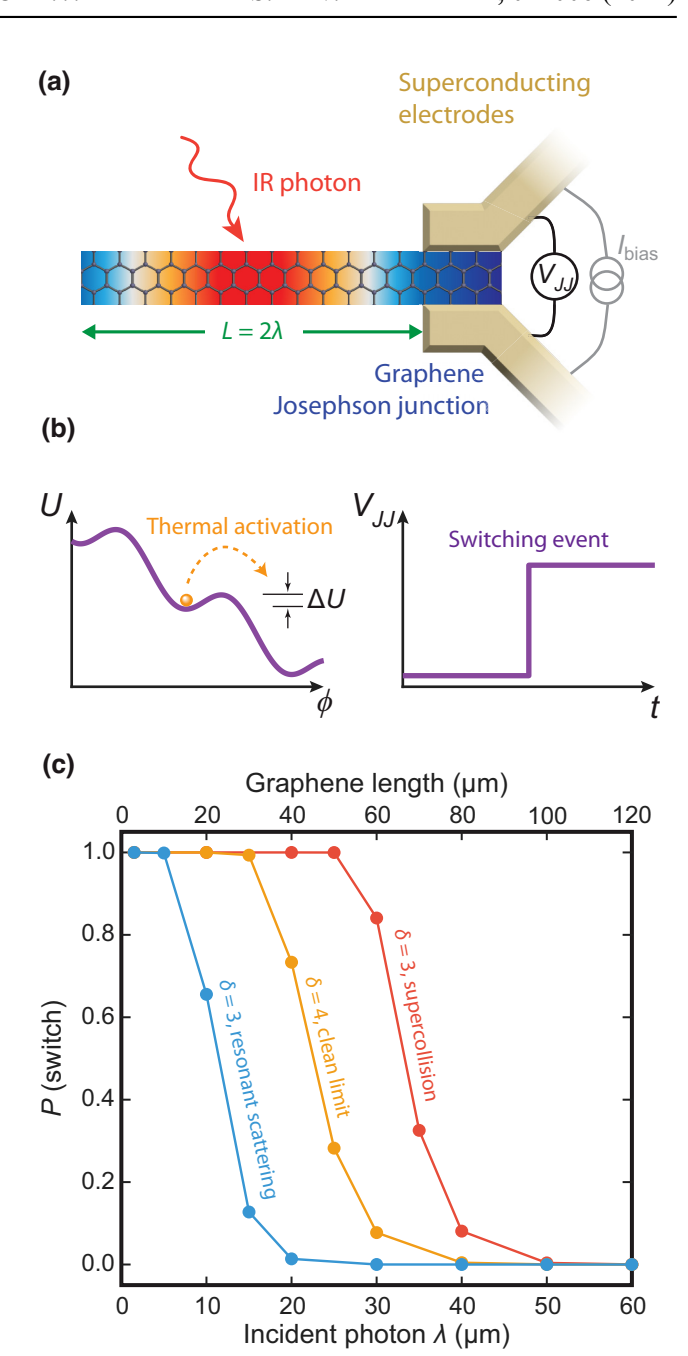


FIG. 7. Josephson junction bolometer performance. (a) A schematic representing a Josephson junction—based bolometer with superconducting readout. The length of the device is set to be the minimum two times the photon wavelength, limited by diffraction. (b) The detection mechanism, whereby thermal fluctuations allow electrons to overcome the washboard potential, leading to thermally activated switching of the Josephson junction detectable via voltage probe. (c) The simulated detection efficiency of such a device for the three *e*-ph coupling regimes, ignoring any geometric losses that might occur from various coupling mechanisms.

absorber. In a longer device, both the diffusive and dissipative parts of Eq. (9) contribute to reduce Θ_e at the sensor position. Additionally, the lower photon energy creates a

lower initial Θ_{hot} , which can be modeled by lowering the photon frequency in Eq. (5) while keeping the hotspot size constant. Our goal in modeling this device is to understand the variation of detection efficiency across a wide range of the electromagnetic spectrum based on this simple design. For the detection of a far-IR photon, which is outside the scope of our discussion, we need to switch from a long graphene absorber to an antenna-coupled device to focus the photon electric field closer to the readout element [50].

We model the graphene-based Josephson junction as a heat switch that changes state due to the heat from absorbing a single photon. This device concept [23] can be understood phenomenologically through the resistively and capacitively shunted junction (RCSJ) model. This model describes Josephson junction dynamics in terms of a fictitious, massive phase particle residing inside the well of a tilted washboard potential that is dependent on the phase difference, ϕ , between the two superconducting electrodes [Fig. 7(b)]. The potential barrier, ΔU , constraining the phase particle is given by $\Delta U = 2E_{I0}(\sqrt{1-\gamma^2} \gamma \cos^{-1} \gamma$), where $E_{J0} = \hbar I_c/2e$ is the Josephson energy and $\gamma = I_b/I_c$, with I_b the applied current bias and I_c the critical current of the junction. While E_{J0} sets the scale of the barrier height, I_b can further tilt the washboard by increasing γ , hence lowering the potential barrier. When the phase particle rests inside the well, the device is in the superconducting state. If, instead, the phase particle is perturbed such that it falls down the well, i.e., with a finite $d\phi/dt$, it is in the normal state. When a photon is absorbed by the graphene, Θ_e rises. With a higher ratio of the thermal energy to the potential barrier, $k_B\Theta_e/\Delta U$, the phase particle can be excited out of the well, causing a transition to the normal state. This transition serves as a heat switch and will result in an increase in the voltage, $V_{\rm JJ}$, measured across the junction [Fig. 7(b)], indicating the detection of a photon. The dark count, i.e., spontaneous switching without incident photons, is predominately caused by macroscopic quantum tunneling [23,42].

Detection of the photon relies on understanding the switching rate of the junction from the superconducting to normal state. When the switching is thermally activated, its rate can be described as

$$\Gamma = Ae^{-\Delta U/k_B\Theta_e},\tag{15}$$

where A is a proportionality factor given by

$$A = \frac{\omega_p}{2\pi} \left(\sqrt{1 + \frac{1}{4Q^2}} - \frac{1}{2Q} \right) \tag{16}$$

with $Q = \omega_p R_n C_{JJ}$ the quality factor of the harmonic well in the washboard potential, where R_n is the junction's normal resistance, C_{JJ} is the junction's capacitance, and ω_p is the plasma frequency of the Josephson junction. At

TABLE III. Parameters of the Josephson junction in our model. These inputs were used along with a fit to an RCSJ model of a Josephson junction to calculate the switching probability from the simulated spatiotemporal temperature response in graphene. These are typical numerical values from experiments [23,42].

Josephson junction device parameters					
Junction capacitance	$C_{ m JJ}$	1.0 fF			
Junction resistance	R	50 Ω			
Critical current	I_c	3.38 μΑ			
Bias current	$I_{ m bias}$	2.80 μΑ			
Quality factor	Q	0.11			
Integration time	$t_{ m meas}$	100 ns			

a finite bias current, $\omega_p = \omega_{p0} (1 - \gamma_{\rm JJ}^2)^{1/4}$, where $\omega_{p0} = \sqrt{2eI_c/\hbar C_{\rm JJ}}$ is the zero-bias plasma frequency.

To calculate the probability of the switching of the Josephson junction from Γ during the duration of the measurement, t_{meas} , we can use [23]

$$P(\text{switch}) = 1 - e^{-\int_0^{t_{\text{meas}}} \Gamma dt}.$$
 (17)

We numerically evaluate P(switch) using the experimental values from a typical graphene-based Josephson junction listed in Table III and plot the results in Fig. 7(c). Regardless of the e-ph coupling regime, we can achieve a high, intrinsic efficiency for short wavelength photons because there is enough photon energy to diffuse to the sensor location through the short graphene absorber. However, as λ lengthens, the efficiency falls as Θ_{hot} decreases. The integral in Eq. (17) signifies that the importance of the temperature response is not only the height of the initial temperature peak, but also the elapsed time that the graphene device remains at elevated temperatures. As such, although the $\delta = 3$ resonant scattering and the $\delta = 4$ clean limit solutions in Fig. 6 appear visually similar, the longer tail of the decaying temperature curve for $\delta = 4$ can significantly impact the thermally activated switching rate, so a device exhibiting $\delta = 4$ behavior is better suited to detecting low-energy photons. Predictably, the $\delta = 3$ supercollision case maintains the highest detector efficiencies at longer photon wavelengths due to its longer time at elevated Θ_e . Similar to Fig. 6, we note that the performance of a single-photon bolometer depends on both the numerical values of Σ and δ in the e-ph coupling, rather than the simple assignment of the e-ph regime. Specifically, we are using Σ and δ from a relatively high-quality graphene in the supercollision regime that is achievable in experiments (Table I).

These results inform the design of single-photon bolometers for different photon detection experiments. For photons with $\lambda < 5~\mu m$, a free-space-coupled single-photon detector should work well, as long as the device is appropriately short. For photons up to 15 μm , the fabrication requirements become more stringent to remain in the

supercollision regime. Finally, if trying to detect photons of $\lambda > 30~\mu m$, some compromises to the photon coupling must be made, or more sophisticated methods must be employed, in both the photon coupling design and device fabrication to maintain a high detection efficiency.

B. Intrinsic limit of jitter due to spatial photonic modes

In addition to detection efficiency, the timing jitter is another important parameter for sensitive photodetectors. The detector physics and process can impose the most fundamental limit to timing jitter [79]. We apply our dissipative heat diffusion model to estimate this intrinsic limit when it is due to the finite size of the spatial mode of the photon input [80].

As described in Sec. II C, the hotspot initially created by absorbing the internal energy of a single photon is effectively a point source. The hotspot can be found anywhere within the beam spot with a probability distribution that follows from the intensity profile of the optical mode. This is because the rate of the photon absorption by graphene is proportional to the square of the electric field, and thus the spatial mode profile. For a diffraction-limited Gaussian beam, we expect the standard deviation of the variation in hotspot location to be of the order of λ .

To calculate time jitter, we use the peak time of Θ_e , t_{max} , in the 1D model, as the time taken for the heat to diffuse from the hotspot to the sensor at a distance d away from the focal point. In Eq. (9), Θ_e hits the peak when

$$t_{\text{max}} = \frac{\sqrt{\mathcal{D}\tau_{e\text{-ph}}(4(d-x_0)^2 + \mathcal{D}\tau_{e\text{-ph}})} - \mathcal{D}\tau_{e\text{-ph}}}{4\mathcal{D}}.$$
 (18)

To estimate the timing jitter, t_{jitter} , we take the difference of t_{max} for $x_0 = \pm \lambda/2$, accounting for the location variation of the hotspot due to photon absorption, such that

$$t_{\text{jitter}} = \frac{1}{4} \sqrt{\frac{\tau_{e\text{-ph}}}{\mathcal{D}}} \left(\sqrt{4(d+\lambda/2)^2 + \mathcal{D}\tau_{e\text{-ph}}} - \sqrt{4(d-\lambda/2)^2 + \mathcal{D}\tau_{e\text{-ph}}} \right). \tag{19}$$

Figure 8(a) plots Eq. (19) versus $\tau_{e\text{-ph}}$. In the diffusive limit, as $\tau_{e\text{-ph}} \to \infty$, t_{max} is determined by the speed of the heat diffusion. Equation (18) reduces to $t_{\text{max}} = (d - x_0)^2 / 2\mathcal{D}$ and the jitter approaches

$$t_{\text{jitter}} = \frac{d\lambda}{\mathcal{D}}.$$
 (20)

Intuitively, the dependence on λ corresponds to a larger spatial uncertainty in photon absorption for longer wavelengths. A short distance, d, or faster diffusion, \mathcal{D} , can reduce the difference of the time taken for the heat to arrive at the sensor from different locations within the

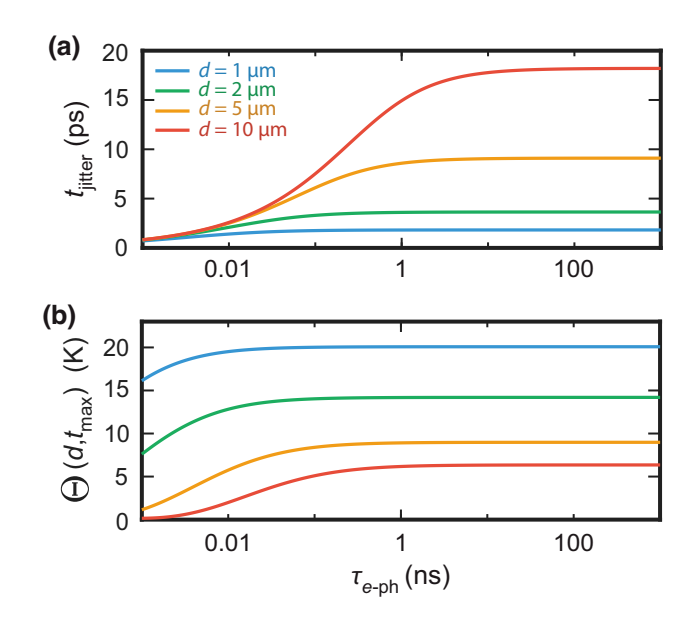


FIG. 8. Dependence of the timing jitter and maximum electron temperature on detector distance. For a graphene single-photon bolometer with $\lambda = 1550$ nm and \mathcal{D} listed in Table I, we plot (a) the timing jitter versus $\tau_{e\text{-ph}}$ according to Eq. (19). In (b), we plot the peak electron temperature at the detector at the time of arrival t_{max} .

spatial mode of the photons. Using $\mathcal{D} = 0.82 \text{ m}^2\text{s}^{-1}$ and taking $d \simeq \lambda$, $t_{\text{iitter}} = 2.7$ ps for 1500-nm wavelength IR photons. This value is comparable to superconducting nanowire single-photon detectors (SNSPDs) [80,81] and can be improved by using higher-mobility graphene or the hydrodynamic effect [34,36]. Paradoxically, Eq. (19) suggests that t_{jitter} also improves at shorter $\tau_{e\text{-ph}}$. This is because the e-ph dissipation tends to reduce t_{max} at the cost of a lower maximum electron temperature, $\Theta_e(x, t_{\text{max}})$ [Fig. 8(b)]. As a result, timing jitter and dissipation are at odds. As the efficiency of a single-photon bolometer relies heavily on a higher $\Theta_e(d,t)$ at the sensor component, it is detrimental to the detector efficiency to improve jitter by increasing the e-ph coupling. For better timing jitter and detector efficiency, the design principle is to operate in the diffusive limit while seeking to maximize \mathcal{D} and minimize d.

VI. QUASI-ONE-DIMENSIONAL MODEL

The previous sections consider the strictly 1D dissipative heat diffusion model with ξ as the effective width suggested by Eq. (11). Here, we would like to understand how the finite width, w, in realistic samples affects our calculations and conclusions. Interestingly, the intuition that we built through the one-dimensional model will help us to approximate a quasi-one-dimensional solution for a narrow rectangular strip, i.e., $w \ll L$ (see Fig. 9).

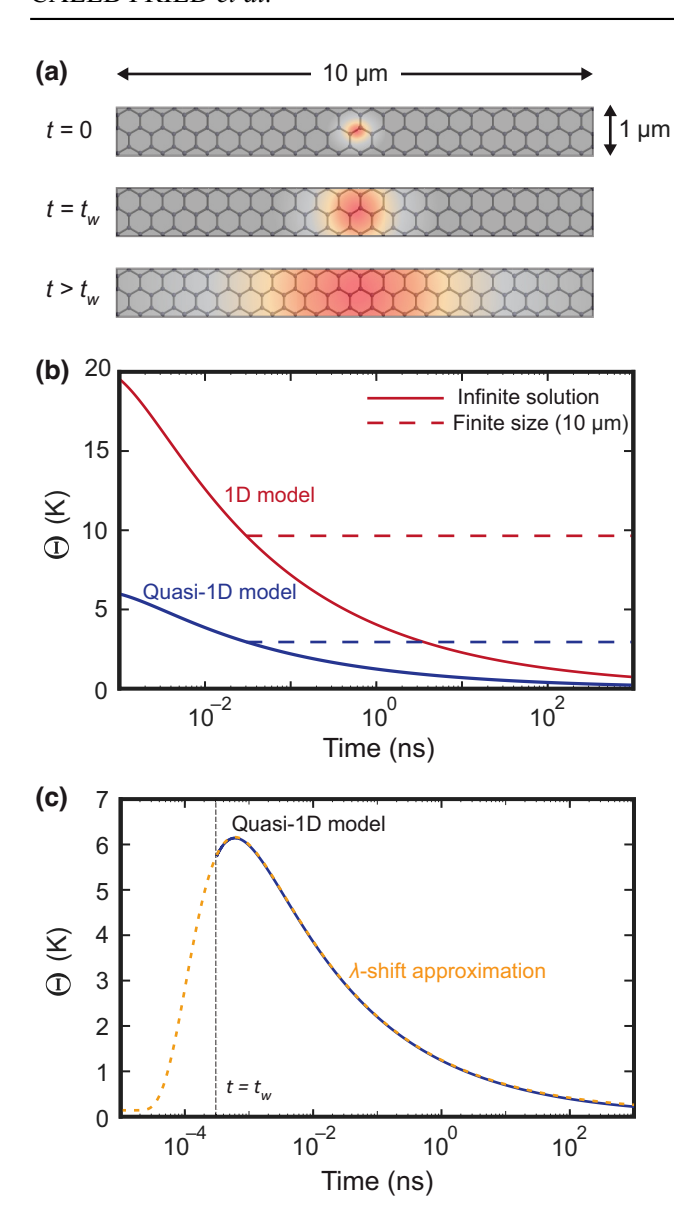


FIG. 9. Quasi-one-dimensional model. (a) The heat diffusion in a quasi-1D graphene system where the width is finite but much shorter than the length. Initially, the heat propagates out in two dimensions, but after a time t_w , the heat has propagated through the full width of the graphene and the system's behavior can be approximated by a 1D solution with a larger and cooler initial hotspot. (b) The different temperature profiles of the 1D versus quasi-1D models for a graphene flake with a length of 10 μ m and a width of 1 μ m, measured at a distance of 1 μ m from the center of the hotspot. (c) Comparison of the quasi-1D solution (black dashed line) with the 1D solution with a lower photon energy (yellow dashed line) as in Eq. (30).

We can extend our 1D initial condition in Eq. (3) to include a second spatial dimension in the transverse direction, *y*:

$$\Theta_e^2(t=0) = \Theta_{\text{hot}}^2 e^{-[(x-x_0)^2 + (y-y_0)^2]/\xi^2} + \Theta_0^2 = \Theta_{\text{hot}}^2 e^{-r^2/\xi^2} + \Theta_0^2$$
 (21)

with the center of the hotspot at (x_0, y_0) . The second equality presents the initial condition in polar coordinates, i.e., $r^2 = (x - x_0)^2 + (y - y_0)^2$. The differential equation and solution of the dissipative heat diffusion in two dimensions is similar to those in one dimension [Eqs. (7) and (9)] and are given by

$$\frac{\partial}{\partial t}\Theta_e^2 = \mathcal{D}\left(\frac{\partial^2}{\partial r^2} + \frac{1}{r}\frac{\partial}{\partial r}\right)\Theta_e^2 - \frac{2\Sigma}{\nu}(\Theta_e^{\delta} - \Theta_0^{\delta}), \quad (22)$$

$$\Theta_e(r,t) = \left[\Theta_0^2 + e^{-t/\tau_{e-ph}} e^{-r^2/(\xi^2 + 4\mathcal{D}t)} \frac{\Theta_{\text{hot}}^2}{1 + 4\mathcal{D}t/\xi^2}\right]^{1/2},$$
(23)

respectively. Qualitatively, our discussions and plots of the solution in one dimension applies in two dimensions as well when the flake is infinitely large [Figs. 3(a)–3(c) and 5] or circular in shape [Figs. 3(d)–3(i), 4, and 6].

When the flake is a strip with $w \ll L$ [Fig. 9(a)], we can construct an approximate, quasi-1D solution. Here Eq. (23) is initially correct before the heat reaches the edge of the graphene flake in the y direction. Similar to the finite width in one dimension, after a characteristic time, t_w , we expect that $\Theta_{\text{2D}}(x=0,y,t)$ becomes uniform in and independent of the y position at the center of the longitudinal direction, provided that $t_w \ll \tau_{e\text{-ph}}$. From our analysis and plots in Fig. 4, $t_w = (w/2)^2/\mathcal{D}$ such that Eq. (23) becomes

$$\Theta_{2D}(x, y, t_{w}) \simeq \left[\Theta_{0}^{2} + e^{-t_{w}/t_{e-ph}} e^{-(x^{2}+y^{2})/(\xi^{2}+w^{2})} \frac{\Theta_{\text{hot}}^{2}}{1 + (w/\xi)^{2}}\right]^{1/2}.$$
(24)

We can now cast the problem back to one dimension by applying Eq. (24) with y = 0 as our new initial condition. Schematically shown as $t = t_w$ in Fig. 9(a), the size of the hotspot at $t = t_w$ should have grown larger than ξ in the new initial condition for our quasi-1D solution. Direct comparison of Eqs. (21) and (24) leads to the definition of the quasi-1D hotspot size, $\tilde{\xi}$, and temperature, $\tilde{\Theta}_{hot}$, as

$$\tilde{\xi} = \sqrt{\xi^2 + w^2},\tag{25}$$

$$\tilde{\Theta}_{\text{hot}} = e^{-t_w/2t_{e\text{-ph}}} \left(\frac{\xi}{\tilde{\xi}}\right) \Theta_{\text{hot}}, \tag{26}$$

respectively. The new quasi-1D initial condition to capture the effect of the finite width of the device is

$$\tilde{\Theta}_{e}^{2}(x,\tilde{t}=0) = \tilde{\Theta}_{\text{hot}}^{2}e^{-x^{2}/\tilde{\xi}^{2}} + \Theta_{0}^{2}, \tag{27}$$

in which we define $\tilde{t} = t - t_w$ as the time reference from the moment, t_w , when Θ_e becomes uniform along the x = 0 center.

Applying this new initial condition, we arrive at the quasi-1D solution

$$\tilde{\Theta}_{e}(x,\tilde{t}) = \left[\Theta_{0}^{2} + e^{-\tilde{t}/\tau_{e\text{-ph}}} e^{-x^{2}/(\tilde{\xi}^{2} + 4\mathcal{D}\tilde{t})} \frac{\tilde{\Theta}_{\text{hot}}^{2}}{\sqrt{1 + 4\mathcal{D}\tilde{t}/\tilde{\xi}^{2}}}\right]^{1/2}.$$
(28)

Analogous to the 1D solution, $\tilde{\xi}$ plays the role of the finite graphene flake width. Figure 9(b) compares the 1D and quasi-1D solutions for $w=1~\mu m$ and infinite $\tau_{e\text{-ph}}$. Specifically, we are interested in $\tilde{\Theta}_e$ for $t\gg \tilde{\xi}^2/4\mathcal{D}$ when the heat has diffused far enough from the hotspot $[t>t_w]$ in Fig. 9(a)]. In this case, we can compute the ratio of the quasi-1D and 1D temperature and find that

$$\frac{\tilde{\Theta}_e}{\Theta_e} \simeq e^{t_w/2\tau_{e\text{-ph}}} \frac{\tilde{\Theta}_{\text{hot}}}{\Theta_{\text{hot}}} \sqrt{\frac{\tilde{\xi}}{\xi}} = \sqrt{\frac{\xi}{\tilde{\xi}}}.$$
 (29)

Therefore, Θ_e and $\tilde{\Theta}_e$ maintain nearly a constant ratio, as shown in Fig. 9(b). The quasi-1D approximate solution in Eq. (28) suggests that, for $t \gg 4\mathcal{D}/\tilde{\xi}^2$, the finite width w will effectively degrade $\Theta_e(x,t)$ by a geometric factor of $\sqrt{\xi/\tilde{\xi}}$ if the dissipation within the time period t_w is negligible.

The $\tilde{\Theta}_e/\Theta_e$ ratio is also helpful to estimate the effect of finite graphene flake width on the detector efficiency as a function of the photon energy that we calculated and plotted in Fig. 7. Although the time integral to calculate the Josephson junction switching probability [Eq. (17)] depends on details of the rise and fall of $\tilde{\Theta}_e$, we can approximate its degradation due to the finite width by observing that, for time $t \gg \tilde{\xi}^2/\mathcal{D}$,

$$\tilde{\Theta}_e \simeq \Theta_e \sqrt{\frac{\xi}{\tilde{\xi}}} \propto \Theta_{\text{hot}} \sqrt{\frac{\xi}{\tilde{\xi}}} \propto hf \sqrt{\frac{\xi}{\tilde{\xi}}},$$
 (30)

based on Eqs. (5) and (10) with $\Theta_{hot} \gg \Theta_0$. This suggests that we can interpret the finite width effect as a reduction of Θ_e [Fig. 9(c)] and the photon energy by the same geometric factor, $\sqrt{\xi/\tilde{\xi}}$. As a result, the detector efficiency for a finite width would simply shift the calculated results in Fig. 7(c) to the left-hand direction by $\sqrt{\xi/\tilde{\xi}}$. In reality, it is an experimental task to fabricate a narrow enough graphene absorber while maintaining a high $\tau_{e\text{-ph}}$ in order to maximize the detector efficiency.

VII. OUTLOOK AND CONCLUSION

The analysis of the dissipative heat diffusion model affirms the feasibility of simultaneously having efficient photon coupling, low-loss heat diffusion, and high-sensitivity superconductor-based readout in an IR graphene bolometer. While the temperature rise and fall in graphene as a function of position and time depends entirely on the detailed parameters, as shown in Fig. 6, we find that a few simple formulas in solving the linearized differential equation can provide a basic understanding of thermal diffusion in the presence of dissipation. Detector performance also depends on the rate of heat dissipation, which varies between e-ph coupling regimes, i.e., supercollision, clean, or resonant scattering. Overall, our device modeling favors the supercollision regime when a longer integration time is needed, for instance to latch a Josephson junction to the normal state. Otherwise, the clean or resonant-scattering e-ph coupling regimes may provide faster reset times due to their faster thermal relaxation in the nonlinear regime. To use our numerical results for a different graphene strip width, we can use a simple geometric factor to find the new detector efficiency.

A better understanding of thermal diffusion and dissipation can lead to photon detectors with expanded functionality. For instance, in Fig. 10 we show a device concept for a spatial-mode-resolving (SMR) detector. With the photon coupling at the center of the graphene flake, comparison of the signals detected by multiple superconducting readouts along the circumference might be able to resolve

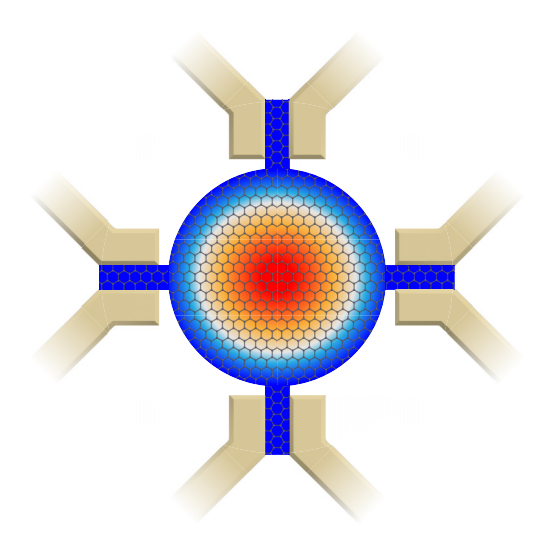


FIG. 10. Device concept of a spatial-mode-resolving detector. Our result points towards the idea that we can exploit the difference in the rise and fall of the electron temperatures at different locations on the graphene flake to resolve the spatial mode of a single photon. Time-resolved measurements of the Josephson junction sensors along the perimeter of the graphene absorber may resolve the location of photon absorption and thus the spatial mode.

the spatial mode of the incident photon. This concept is analogous to temporal sensing in SNSPDs, where the location of the hotspot in the nanowire can be detected by two amplifiers at opposite ends. Compared to the recent demonstration of an SNSPD camera [82], graphene-based SMR detectors may have a larger spectral bandwidth for longer-wavelength photons. As a single photon can carry a large amount of quantum information by exploiting the multiple degrees of freedom in its spatial, temporal, and polarization modes, an SMR detector could provide a much needed technical capability in computation and communication based on single-photon quantum logic.

ACKNOWLEDGMENTS

We thank J. Balgley, M. Kreidel, and J. Park for helpful discussions. B.J.R. and E.A.H. acknowledge support under NSF CAREER DMR-1945278 and the Center for Quantum Leaps, Washington University in St. Louis. B.H. acknowledges that this research was supported by an appointment to the Intelligence Community Postdoctoral Research Fellowship Program at the Massachusetts Institute of Technology, administered by Oak Ridge Institute for Science and Education through an interagency agreement between the U.S. Department of Energy and the Office of the Director of National Intelligence. E.G.A. acknowledges support from the Army Research Office MURI (Ab-Initio Solid-State Quantum Materials) under Grant No. W911NF-18-1-043. G.-H.L. was supported by the ITRC program (IITP-2022-RS-2022-00164799) and NRF grants (No. 2021R1A6A1A10042944, No. 2022M3H4A1A04074153 and No. RS-2023-00207732) funded by the Ministry of Science and ICT. This work was funded in part by NRO Contract NRO000-20-C-0256. All findings and opinions expressed herein are those of the authors and not the U.S. Government.

- [1] S. Pirro and P. Mauskopf, Advances in bolometer technology for fundamental physics, Annu. Rev. Nucl. Part. Sci. **67**, 161 (2017).
- [2] J. Schütte-Engel *et al.*, Axion quasiparticles for axion dark matter detection (2021).
- [3] A. M. Gunyhó *et al.*, Single-shot readout of a superconducting qubit using a thermal detector. arXiv (2023).
- [4] C. Couteau, S. Barz, T. Durt, T. Gerrits, J. Huwer, R. Prevedel, J. Rarity, A. Shields, and G. Weihs, Applications of single photons in quantum metrology, biology and the foundations of quantum physics, Nat. Rev. Phys. 5, 354 (2023)
- [5] V. Ryzhii, T. Otsuji, M. Ryzhii, N. Ryabova, S. O. Yurchenko, V. Mitin, and M. S. Shur, Graphene terahertz uncooled bolometers, J. Phys. D: Appl. Phys. 46, 065102 (2013).
- [6] X. Cai, A. B. Sushkov, R. J. Suess, M. M. Jadidi, G. S. Jenkins, L. O. Nyakiti, R. L. Myers-Ward, S. Li, J. Yan,

- D. K. Gaskill, T. E. Murphy, H. D. Drew, and M. S. Fuhrer, Sensitive room-temperature terahertz detection via the photothermoelectric effect in graphene, Nat. Nanotechnol. 9, 814 (2014).
- [7] A. E. Fatimy, R. L. Myers-Ward, A. K. Boyd, K. M. Daniels, D. K. Gaskill, and P. Barbara, Epitaxial graphene quantum dots for high-performance terahertz bolometers, Nat. Nanotechnol. 11, 335 (2016).
- [8] U. Sassi, R. Parret, S. Nanot, M. Bruna, S. Borini, D. De Fazio, Z. Zhao, E. Lidorikis, F. H. L. Koppens, A. C. Ferrari, and A. Colli, Graphene-based mid-infrared room-temperature pyroelectric bolometers with ultrahigh temperature coefficient of resistance, Nat. Commun. 8, 14311 (2017).
- [9] A. Zoghi and H. R. Saghai, Enhancing performance of graphene-based bolometers at 1 THz, Physica C: Superconductivity and its Applications 557, 44 (2019).
- [10] A. Blaikie, D. Miller, and B. J. Alemán, A fast and sensitive room-temperature graphene nanomechanical bolometer, Nat. Commun. 10, 1 (2019).
- [11] Y. Xie, M. Han, R. Wang, H. Zobeiri, X. Deng, P. Zhang, and X. Wang, Graphene aerogel based bolometer for ultrasensitive sensing from ultraviolet to far-infrared, ACS Nano 13, 5385 (2019).
- [12] W. Miao, H. Gao, Z. Wang, W. Zhang, Y. Ren, K. M. Zhou, S. C. Shi, C. Yu, Z. Z. He, Q. B. Liu, and Z. H. Feng, A graphene-based terahertz hot electron bolometer with Johnson noise readout, J. Low Temp. Phys. 193, 387 (2018).
- [13] G. Skoblin, J. Sun, and A. Yurgens, Graphene bolometer with thermoelectric readout and capacitive coupling to an antenna, Appl. Phys. Lett. **112**, 063501 (2018).
- [14] R. Haller, G. Fülöp, D. Indolese, J. Ridderbos, R. Kraft, L. Y. Cheung, J. H. Ungerer, K. Watanabe, T. Taniguchi, D. Beckmann, R. Danneau, P. Virtanen, and C. Schönenberger, Phase-dependent microwave response of a graphene Josephson junction, Phys. Rev. Res. 4, 013198 (2022).
- [15] H. Chen et al., Gate-tunable bolometer based on strongly coupled graphene mechanical resonators, Opt. Lett. 48, 81 (2022).
- [16] H. Vora, P. Kumaravadivel, B. Nielsen, and X. Du, Bolometric response in graphene based superconducting tunnel junctions, Appl. Phys. Lett. **100**, 153507 (2012).
- [17] J. Yan, M-H. Kim, J. A. Elle, A. B. Sushkov, G. S. Jenkins, H. M. Milchberg, M. S. Fuhrer, and H. D. Drew, Dual-gated bilayer graphene hot-electron bolometer, Nat. Nanotechnol. 7, 472 (2012).
- [18] K. C. Fong and K. Schwab, Ultrasensitive and wide-bandwidth thermal measurements of graphene at low temperatures, Phys. Rev. X 2, 031006 (2012).
- [19] G.-H. Lee, D. K. Efetov, W. Jung, L. Ranzani, E. D. Walsh, T. A. Ohki, T. Taniguchi, K. Watanabe, P. Kim, D. Englund, and K. C. Fong, Graphene-based Josephson junction microwave bolometer, Nature 586, 42 (2020).
- [20] R. Kokkoniemi, J.-P. Girard, D. Hazra, A. Laitinen, J. Govenius, R. E. Lake, I. Sallinen, V. Vesterinen, M. Partanen, J. Y. Tan, K. W. Chan, K. Y. Tan, P. Hakonen, and M. Möttönen, Bolometer operating at the threshold for circuit quantum electrodynamics, Nature 586, 47 (2020).

- [21] P. Seifert *et al.*, Magic-angle bilayer graphene nano-calorimeters: Toward broadband, energy-resolving single photon detection, Nano Lett. **20**, 3459 (2020).
- [22] G. D. Battista, P. Seifert, K. Watanabe, T. Taniguchi, K. C. Fong, A. Principi, and D. K. Efetov, Revealing the thermal properties of superconducting magic-angle twisted bilayer graphene, Nano Lett. 22, 6465 (2022).
- [23] E. D. Walsh, D. K. Efetov, G.-H. Lee, M. Heuck, J. Crossno, T. A. Ohki, P. Kim, D. Englund, and K. C. Fong, Graphene-based Josephson-junction single-photon detector, Phys. Rev. Appl. 8, 024022 (2017).
- [24] J. P. Pekola and B. Karimi, Ultrasensitive calorimetric detection of single photons from qubit decay, Phys. Rev. X 12, 011026 (2022).
- [25] M. A. Aamir *et al.*, Ultrasensitive calorimetric measurements of the electronic heat capacity of graphene, Nano Lett. 21, 5330 (2021).
- [26] S. D. Sarma, S. Adam, E. H. Hwang, and E. Rossi, Electronic transport in two-dimensional graphene, Rev. Mod. Phys. 83, 407 (2011).
- [27] E. H. Hwang and S. D. Sarma, Acoustic phonon scattering limited carrier mobility in two-dimensional extrinsic graphene, Phys. Rev. B 77, 115449 (2008).
- [28] R. Bistritzer and A. H. Macdonald, Electronic cooling in graphene, Phys. Rev. Lett. 102, 206410 (2009).
- [29] S. S. Kubakaddi, Interaction of massless Dirac electrons with acoustic phonons in graphene at low temperatures, Phys. Rev. B 79, 075417 (2009).
- [30] J. K. Viljas and T. T. Heikkila, Electron-phonon heat transfer in monolayer and bilayer graphene, Phys. Rev. B 81, 245404 (2010).
- [31] J. C. W. Song and L. S. Levitov, Energy-driven drag at charge neutrality in graphene, Phys. Rev. Lett. 109, 236602 (2012).
- [32] W. Chen and A. A. Clerk, Electron-phonon mediated heat flow in disordered graphene, Phys. Rev. B 86, 670 (2012).
- [33] M. Massicotte, G. Soavi, A. Principi, and K.-J. Tielrooij, Hot carriers in graphene – fundamentals and applications, Nanoscale 13, 8376 (2021).
- [34] A. Lucas and K. C. Fong, Hydrodynamics of electrons in graphene (2017).
- [35] P. Gallagher, C.-S. Yang, T. Lyu, F. Tian, R. Kou, H. Zhang, K. Watanabe, T. Taniguchi, and F. Wang, Quantum-critical conductivity of the Dirac fluid in graphene, Science 364, 158 (2019).
- [36] A. Block, A. Principi, N. C. H. Hesp, A. W. Cummings, M. Liebel, K. Watanabe, T. Taniguchi, S. Roche, F. H. L. Koppens, N. F. van Hulst, and K.-J. Tielrooij, Observation of giant and tunable thermal diffusivity of a Dirac fluid at room temperature, Nat. Nanotechnol. 16, 1195 (2021)
- [37] J. C. W. Song, M. S. Rudner, C. M. Marcus, and L. S. Levitov, Hot carrier transport and photocurrent response in graphene, Nano Lett. 11, 4688 (2011).
- [38] K. J. Tielrooij, J. C. W. Song, S. A. Jensen, A. Centeno, A. Pesquera, A. Zurutuza Elorza, M. Bonn, L. S. Levitov, and F. H. L. Koppens, Photoexcitation cascade and multiple hot-carrier generation in graphene, Nat. Phys. 9, 248 (2013).

- [39] X. Du, D. E. Prober, H. Vora, and C. B. Mckitterick, Graphene-based bolometers, Graphene and 2D Materials 1 (2014).
- [40] D. K. Efetov, R.-J. Shiue, Y. Gao, B. Skinner, E. D. Walsh, H. Choi, J. Zheng, C. Tan, G. Grosso, C. Peng, J. Hone, K. C. Fong, and D. Englund, Fast thermal relaxation in cavitycoupled graphene bolometers with a Johnson noise readout, Nat. Nanotechnol. 13, 797 (2018).
- [41] Q. Han, T. Gao, R. Zhang, Y. Chen, J. Chen, G. Liu, Y. Zhang, Z. Liu, X. Wu, and D. Yu, Highly sensitive hot electron bolometer based on disordered graphene, Sci. Rep. 3, 3533 (2013).
- [42] E. D. Walsh, W. Jung, G.-H. Lee, D. K. Efetov, B.-I. Wu, K.-F. Huang, T. A. Ohki, T. Taniguchi, K. Watanabe, P. Kim, D. Englund, and K. C. Fong, Josephson junction infrared single-photon detector, Science 372, 409 (2021).
- [43] R. Katti *et al.*, Hot carrier thermalization and Josephson inductance thermometry in a graphene-based microwave circuit. arXiv (2022).
- [44] B. A. Ruzicka *et al.*, Hot carrier diffusion in graphene, Phys. Rev. B **82**, 195414 (2010).
- [45] D. Brida, A. Tomadin, C. Manzoni, Y. J. Kim, A. Lombardo, S. Milana, R. R. Nair, K. S. Novoselov, A. C. Ferrari, G. Cerullo, and M. Polini, Ultrafast collinear scattering and carrier multiplication in graphene, Nat. Commun. 4, 1987 (2013).
- [46] R. Jago, R. Perea-Causin, S. Brem, and E. Malic, Spatiotemporal dynamics in graphene, Nanoscale 11, 10017 (2019).
- [47] A. W. Draelos, A. Silverman, B. Eniwaye, E. G. Arnault, C. T. Ke, M. T. Wei, I. Vlassiouk, I. V. Borzenets, F. Amet, and G. Finkelstein, Subkelvin lateral thermal transport in diffusive graphene, Phys. Rev. B 99, 125427 (2019).
- [48] B. Vasić and R. Gajić, Tunable Fabry–Perot resonators with embedded graphene from terahertz to near-infrared frequencies, Opt. Lett. **39**, 6253 (2014).
- [49] J. Wang, Z. Xing, X. Chen, Z. Cheng, X. Li, and T. Liu, Recent progress in waveguide-integrated graphene photonic devices for sensing and communication applications, Front. Phys. 8, 37 (2020).
- [50] S. Castilla, B. Terrés, M. Autore, L. Viti, J. Li, A. Y. Nikitin, I. Vangelidis, K. Watanabe, T. Taniguchi, E. Lidorikis *et al.*, Fast and sensitive terahertz detection using an antennaintegrated graphene pn junction, Nano Lett. 19, 2765 (2019).
- [51] J. C. Johannsen *et al.*, Direct view of hot carrier dynamics in graphene, Phys. Rev. Lett. 111, 027403 (2013).
- [52] R. Somphonsane, H. Ramamoorthy, G. Bohra, G. He, D. K. Ferry, Y. Ochiai, N. Aoki, and J. P. Bird, Fast energy relaxation of hot carriers near the Dirac point of graphene, Nano Lett. 13, 4305 (2013).
- [53] I. J. Vera-Marun, J. J. v. d. Berg, F. K. Dejene, and B. J. v. Wees, Direct electronic measurement of Peltier cooling and heating in graphene, Nat. Commun. 7, 11525 (2016).
- [54] N. M. Gabor, J. C. W. Song, Q. Ma, N. L. Nair, T. Tay-chatanapat, K. Watanabe, T. Taniguchi, L. S. Levitov, and P. Jarillo-Herrero, Hot carrier-assisted intrinsic photoresponse in graphene, Science **334**, 648 (2011).
- [55] R. Rengel, E. Pascual, and M. J. Martín, Influence of the substrate on the diffusion coefficient and the momentum

- relaxation in graphene: The role of surface polar phonons, Appl. Phys. Lett. **104**, 233107 (2014).
- [56] J. Crossno, X. Liu, T. A. Ohki, P. Kim, and K. C. Fong, Development of high frequency and wide bandwidth Johnson noise thermometry, Appl. Phys. Lett. 106, 023121 (2015).
- [57] H. L. Stormer, L. N. Pfeiffer, K. W. Baldwin, and K. W. West, Observation of a Bloch-Grüneisen regime in two-dimensional electron transport, Phys. Rev. B 41, 1278 (1990).
- [58] D. K. Efetov and P. Kim, Controlling electron-phonon interactions in graphene at ultra high carrier densities. arXiv cond-mat.mes-hall (2010).
- [59] A. C. Betz *et al.*, Hot electron cooling by acoustic phonons in graphene, Phys. Rev. Lett. **109**, 056805 (2012).
- [60] C. B. McKitterick, D. E. Prober, and M. J. Rooks, Electronphonon cooling in large monolayer graphene devices, Phys. Rev. B 93, 075410 (2016).
- [61] M. W. Graham, S.-F. Shi, D. C. Ralph, J. Park, and P. L. McEuen, Photocurrent measurements of supercollision cooling in graphene, Nat. Phys. 9, 103 (2013).
- [62] A. C. Betz *et al.*, Supercollision cooling in undoped graphene, Nat. Phys. **9**, 109 (2013).
- [63] K. C. Fong, Emma E. Wollman, Harish Ravi, Wei Chen, Aashish A. Clerk, M. D. Shaw, H. G. Leduc, and K. C. Schwab, Measurement of the electronic thermal conductance channels and heat capacity of graphene at low temperature, Phys. Rev. X 3, 041008 (2013).
- [64] Q. Ma, N. M. Gabor, T. I. Andersen, N. L. Nair, K. Watanabe, T. Taniguchi, and P. Jarillo-Herrero, Competing channels for hot-electron cooling in graphene, Phys. Rev. Lett. 112, 247401 (2014).
- [65] T. O. Wehling, S. Yuan, A. I. Lichtenstein, A. K. Geim, and M. I. Katsnelson, Resonant scattering by realistic impurities in graphene, Phys. Rev. Lett. 105, 056802 (2010).
- [66] D. Halbertal, M. B. Shalom, A. Uri, K. Bagani, A. Y. Meltzer, I. Marcus, Y. Myasoedov, J. Birkbeck, L. S. Levitov, A. K. Geim, and E. Zeldov, Imaging resonant dissipation from individual atomic defects in graphene, Science 358, 1303 (2017).
- [67] J. F. Kong, L. Levitov, D. Halbertal, and E. Zeldov, Resonant electron-lattice cooling in graphene, Phys. Rev. B 97, 245416 (2018).
- [68] A. W. Draelos, M.-T. Wei, A. Seredinski, H. Li, Y. Mehta, K. Watanabe, T. Taniguchi, I. V. Borzenets, F. Amet, and G. Finkelstein, Supercurrent flow in multiterminal graphene Josephson junctions, Nano Lett. 19, 1039 (2019).
- [69] V. Eless, T. Yager, S. Spasov, S. Lara-Avila, R. Yakimova, S. Kubatkin, T. J. B. M. Janssen, A. Tzalenchuk, and V. Antonov, Phase coherence and energy relaxation in epitax-

- ial graphene under microwave radiation, Appl. Phys. Lett. **103**, 093103 (2013).
- [70] C. B. Satterthwaite, Thermal conductivity of normal and superconducting aluminum, Phys. Rev. 125, 873 (1962).
- [71] J. C. W. Song, K. J. Tielrooij, F. H. L. Koppens, and L. S. Levitov, Photoexcited carrier dynamics and impactexcitation cascade in graphene, Phys. Rev. B 87, 155429 (2013).
- [72] S. Ulstrup, J. C. Johannsen, A. Crepaldi, F. Cilento, M. Zacchigna, C. Cacho, R. T. Chapman, E. Springate, F. Fromm, C. Raidel *et al.*, Ultrafast electron dynamics in epitaxial graphene investigated with time- and angle-resolved photoemission spectroscopy, J. Phys. Condens. Matter 27, 164206 (2015).
- [73] J. C. W. Song, D. A. Abanin, and L. S. Levitov, Coulomb drag mechanisms in graphene, Nano Lett. 13, 3631 (2013).
- [74] R. Rengel and M. J. Martín, Diffusion coefficient, correlation function, and power spectral density of velocity fluctuations in monolayer graphene, J. Appl. Phys. 114, 143702 (2013).
- [75] S. Gasparinetti, K. L. Viisanen, O.-P. Saira, T. Faivre, M. Arzeo, M. Meschke, and J. P. Pekola, Fast electron thermometry for ultrasensitive calorimetric detection, Phys. Rev. Appl. 3, 014007 (2015).
- [76] M. Zgirski, M. Foltyn, A. Savin, K. Norowski, M. Meschke, and J. Pekola, Nanosecond thermometry with Josephson junctions, Phys. Rev. Appl. 10, 044068 (2018).
- [77] F. Giazotto, Tero T. Heikkilä, Giovanni Piero Pepe, Panu Helistö, Arttu Luukanen, and Jukka P. Pekola, Ultrasensitive proximity Josephson sensor with kinetic inductance readout, Appl. Phys. Lett. 92, 162507 (2008).
- [78] M. Ye, J. Zha, C. Tan, and K. B. Crozier, Graphene-based mid-infrared photodetectors using metamaterials and related concepts, Appl. Phys. Rev. 8, 031303 (2021).
- [79] J. Allmaras, A. Kozorezov, B. Korzh, K. Berggren, and M. Shaw, Intrinsic timing jitter and latency in superconducting nanowire single-photon detectors, Phys. Rev. Appl. 11, 034062 (2019).
- [80] B. Korzh *et al.*, Demonstration of sub-3 ps temporal resolution with a superconducting nanowire single-photon detector, Nat. Photonics **14**, 250 (2020).
- [81] I. E. Zadeh *et al.*, Efficient single-photon detection with 7.7 ps time resolution for photon-correlation measurements, ACS Photonics 7, 1780 (2020).
- [82] B. G. Oripov, D. S. Rampini, J. Allmaras, M. D. Shaw, S. W. Nam, B. Korzh, and A. N. McCaughan, A superconducting nanowire single-photon camera with 400 000 pixels, Nature 622, 730 (2023).